Journal of Computational Physics 228 (2009) 6426–6439

Contents lists available at ScienceDirect

Journal of Computational Physics

journal homepage: www.elsevier.com/locate/jcp

Numerical simulation of Rhonegletscher from 1874 to 2100

Guillaume Jouvet [a,1], Matthias Huss [b], Heinz Blatter [c], Marco Picasso [a,*], Jacques Rappaz [a]

[a] Institut d'Analyse et Calcul Scientifique, EPFL,1015 Lausanne, Switzerland
[b] Laboratory of Hydraulics, Hydrology and Glaciology (VAW), ETH Zurich, 8092 Zurich, Switzerland
[c] Institute for Atmospheric and Climate Science, ETH Zurich, 8092 Zurich, Switzerland

ARTICLE INFO

Article history:
Received 10 November 2008
Received in revised form 13 May 2009
Accepted 14 May 2009
Available online 27 May 2009

Keywords:
Ice flow
Finite elements
Volume of fluid
Free surface

ABSTRACT

Due to climatic change, many Alpine glaciers have significantly retreated during the last century. In this study we perform the numerical simulation of the temporal and spatial change of Rhonegletscher, Swiss Alps, from 1874 to 2007, and from 2007 to 2100.

Given the shape of the glacier, the velocity of ice **u** is obtained by solving a 3D nonlinear Stokes problem with a nonlinear sliding law along the bedrock–ice interface. The shape of the glacier is updated by computing the volume fraction of ice φ, which satisfies a transport equation. The accumulation due to snow fall and the ablation due to melting is accounted by adding a source term to the transport equation.

A decoupling algorithm allows the two above problems to be solved using different numerical techniques. The nonlinear Stokes problem is solved on a fixed, unstructured finite element mesh consisting of tetrahedrons. The transport equation is solved using a fixed, structured grid of smaller cells.

The numerical simulation, from 1874 to 2007, is validated against measurements. Afterwards, three different climatic scenarios are considered in order to predict the shape of Rhonegletscher until 2100. A dramatic retreat of Rhonegletscher during the 21st century is anticipated. Our results contribute to a better understanding of the impact of climatic change on mountain glaciers.

1. Introduction

Glaciers are relevant not only for tourism but also for the future management of natural risks, hydroelectric plants and water supply for agriculture. Earth is in a warm, interglacial period, exacerbated by global warming resulting in the retreat of the glaciers [19]. Since the end of the 19th century, glaciologists have documented the retreat of the glaciers in the Swiss Alps (e.g. [23]).

The dynamics of a glacier are the result of different phenomena. In the upper part of the glacier snow fall exceeds snow melt (accumulation), whereas icemelt is preponderant in the lower reaches of the glacier (ablation) because of higher temperatures. Due to gravity, ice is flowing downvalley. When studying ice flow during years or centuries, ice can be considered as an incompressible non-Newtonian fluid, governed by the mass and momentum conservation in the limit of a stationary nonlinear Stokes flow. A sliding law is added on the bedrock to account for the basal motion. Mass conservation along the ice–air interface yields a transport equation which can be used to determine the evolution of the glacier shape. A source term – the so-called mass balance – must be added to the right hand side of this transport equation in order to take into account

* Corresponding author.
E-mail address: marco.picasso@epfl.ch (M. Picasso).
[1] Supported by the Swiss National Science Foundation.

0021-9991/$ - see front matter © 2009 Elsevier Inc. All rights reserved.
doi:10.1016/j.jcp.2009.05.033

accumulation or ablation. This term contains the climatic input of the model and several scenarios can be explored in order to predict the future retreat of Alpine glaciers.

Most of the numerical simulations presented so far in glaciology have been performed using Lagrangian or Arbitrary Lagrangian Eulerian methods, see for instance [5] or [27]. When considering ice flow during centuries, topological changes may appear so that Eulerian methods such as Level Set [25] or Volume of Fluid (VOF) [29] seem to be more appropriate. Level set methods in glaciology have been considered in [28] to compute the onset of crevasse formation in 2D. The VOF formulation has been used in [20] to reconstruct stationary 3D glacier shapes.

In this paper, the different states of Rhonegletscher, Switzerland, are reconstructed in 3D over the period 1874–2007 and predictions for the coming century are given. The evolution of Rhonegletscher in the past and in the future has previously been studied using a flowline model and simple parametrizations of mass balance [32,34]. The determination of the glacier surface mass balance over 133 years results from a combination of long-term measurements, performed by glaciologists, and a parameter identification procedure that involves climate data and observations of surface elevation change [16]. Using the mass balance data and the measured bedrock elevation [7] as boundary conditions the three dimensional ice flow model is run for the period 1874 to 2007. The results of these simulations are compared to direct measurements. Based on climate models in seasonal resolution [9], three climatic scenarios are defined allowing the computation of future mass balances [17]. In combination with the 3D ice flow model, the future shape of Rhonegletscher is calculated from 2007 to 2100.

The paper is organized as follows: The mathematical model is presented in the next section and corresponds to the model already presented in [20]. Boundary conditions are introduced that allow sliding along the bedrock–ice interface. The numerical procedure presented in Section 3 also corresponds to [20]. At each time step, the velocity computation is decoupled from the glacier shape computation, which allows different numerical techniques to be used for solving each of these two subproblems (see [1,3,22]). The computation of the mass balance is presented in Section 4 and follows a method described in [16]. Finally, numerical results are presented in Section 5. The question of sliding boundary conditions is discussed and numerical results are compared to measured changes in glacier length during the last century. Finally, forecasts for Rhonegletscher's evolution until 2100, based on three different climatic scenarios [17], are reported.

2. The mathematical model

We are interested in computing the shape of a glacier between time $t = 0$ and $t = T$. Let Λ be a cavity of $\mathbb{R}^3$ in which the ice domain is contained, see Fig. 1. At time t the ice domain is denoted by $\Omega(t)$, the bedrock–ice interface is $\Gamma_B(t)$ and the ice–air interface is $\Gamma_A(t)$. Let Q_T be the ice region in the space-time domain:

$$Q_T = \{(x, y, z, t) \in \Lambda \times (0, T); (x, y, z) \in \Omega(t); 0 < t < T\},$$

and let $\mathbf{u} = (u, v, w) : Q_T \to \mathbb{R}^3$ and $p : Q_T \to \mathbb{R}$ be the ice velocity and pressure, respectively. When considering the motion of a glacier during years or centuries, ice can be considered as an incompressible non-Newtonian fluid. Moreover, a dimensionless scaling shows that inertial terms can be disregarded. Therefore, the mass and momentum equations reduce at time t to a stationary nonlinear Stokes problem in the ice domain $\Omega(t)$:

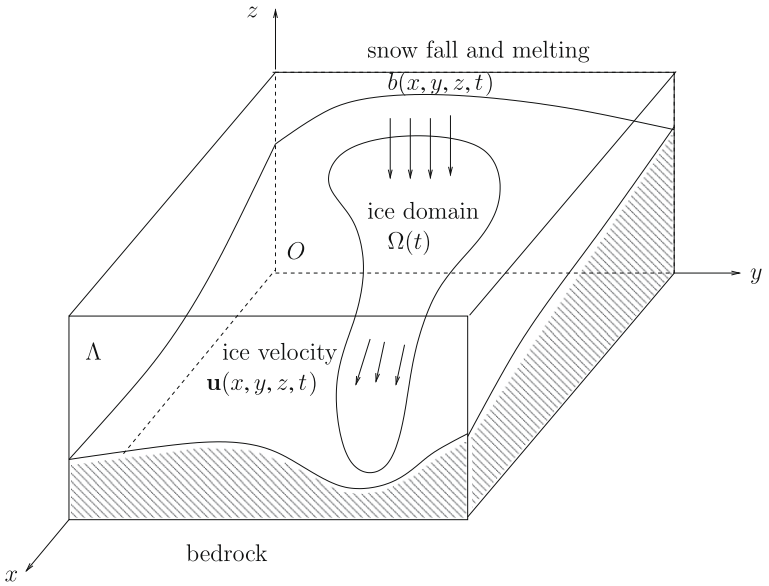

Fig. 1. Notations. For convenience, the bedrock–ice interface $\Gamma_B(t)$ and the ice–air interface $\Gamma_A(t)$ are not represented.

$$-2\mathrm{div}(\mu\varepsilon(\mathbf{u})) + \nabla p = \rho\mathbf{g}, \tag{1}$$

$$\mathrm{div}\,\mathbf{u} = 0. \tag{2}$$

Hereabove $\varepsilon(\mathbf{u}) = \frac{1}{2}(\nabla\mathbf{u} + \nabla\mathbf{u}^T)$ denotes the rate of strain rank 2 tensor and Glen's flow law [13,18] holds for the viscosity $\mu = \mu(\mathbf{u})$. More precisely, for a given velocity field $\mathbf{u}$, the viscosity μ satisfies the following nonlinear equation:

$$\frac{1}{2\mu} = A\left(\sigma_0^{m-1} + \left(2\mu\sqrt{\frac{1}{2}(\varepsilon(\mathbf{u}) : \varepsilon(\mathbf{u}))}\right)^{m-1}\right), \tag{3}$$

where A is a positive number known as the rate factor, $m \geqslant 1$ is Glen's exponent and $\sigma_0 > 0$ is a small regularization parameter which prevents infinite viscosity for zero strain ($\sigma_0 = 0$ in the original Glen's law). It should be noted that A depends on ice temperature but, since temperature varies very little in most Alpine glaciers, A can be taken as a constant for Rhonegletscher. When $m > 1$, it is shown in [4] that μ is a positive, strictly decreasing function with respect to $s := \sqrt{\frac{1}{2}(\varepsilon(\mathbf{u}) : \varepsilon(\mathbf{u}))}$. The viscosity μ is upper-bounded by its value at $s = 0$ and has the following asymptotic behaviour when s goes to the infinity:

$$\mu(s) = O(s^{\frac{1}{m}-1}). \tag{4}$$

When $m = 1$, then μ is constant and the above problem corresponds to a Newtonian fluid. In the framework of glaciology, m is often taken equal to 3 [14], then Eq. (3) can be solved exactly using the Cardan formula, see Fig. 2.

The boundary conditions corresponding to (1) are the following. Since no force applies on the ice–air interface $\Gamma_A(t)$:

$$2\mu\varepsilon(\mathbf{u})\cdot\mathbf{n} - p\mathbf{n} = \mathbf{0}, \tag{5}$$

where $\mathbf{n}$ is the unit outer normal vector along the boundary of the ice domain $\Omega(t)$. Along the bedrock–ice interface $\Gamma_B(t)$, ice may slip or not, according to the bedrock characteristics. Many sliding laws have been proposed, see for instance [8] for a derivation from first principles and [11,30,33,31] for recent contributions. A nonlinear law relating the tangent stress to the tangent velocity is considered here. Let $\Gamma_B^S(t)$, $\Gamma_B^{NS}(t)$ be the portion of the bedrock–ice interface where slip, no-slip occurs, respectively. The no-slip condition writes

$$\mathbf{u} = \mathbf{0} \quad \text{on } \Gamma_B^{NS}(t), \tag{6}$$

whereas the slip condition is:

$$\mathbf{u}\cdot\mathbf{n} = 0 \quad \text{and} \quad (2\mu\varepsilon(\mathbf{u})\cdot\mathbf{n})\cdot\mathbf{t}_i = -\alpha\mathbf{u}\cdot\mathbf{t}_i \quad i = 1,2 \text{ on } \Gamma_B^S(t), \tag{7}$$

where $\mathbf{t}_1$, $\mathbf{t}_2$ are two orthogonal vectors tangent to the boundary $\Gamma_B^S(t)$. Hereabove, following [18, p. 454], $\alpha = \alpha(\mathbf{u})$ is the sliding coefficient that is given by

$$\alpha = \frac{C}{\left(\sqrt{u^2 + v^2 + w^2} + s_0\right)^{1-\frac{1}{m}}}, \tag{8}$$

where m is the Glen exponent, C is a positive value tuned from experiments and s_0 is a small numerical parameter which prevents infinite α for zero velocity.

The well-posedness of the nonlinear Stokes problem (1)–(3) supplemented by the boundary conditions (5), (6) in a prescribed smooth domain Ω can be proved using the property (4), proceeding as in [4]. Please note that a similar result is proved in [31], even when Γ_B^{NS} is empty.

We now turn to the model for the volume fraction of ice. As in [20], the presence of ice is described by the characteristic function $\varphi : \Lambda \times (0,T) \to \mathbb{R}$ defined by:

$$\varphi(x,y,z,t) = \begin{cases} 1, & \text{if } (x,y,z) \in \Omega(t), \\ 0, & \text{else.} \end{cases} \tag{9}$$

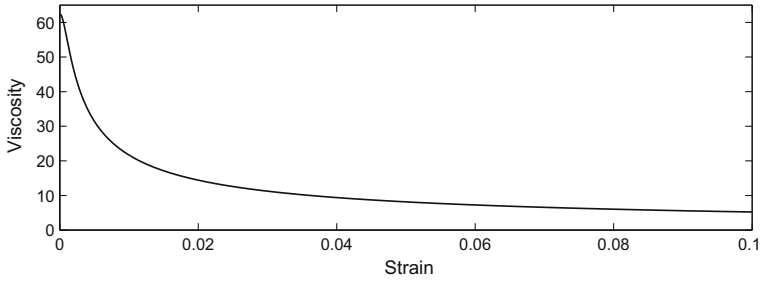

Fig. 2. Viscosity (unit: bar a) with respect to the strain's norm $\sqrt{\frac{1}{2}(\varepsilon(\mathbf{u}) : \varepsilon(\mathbf{u}))}$ (unit: a^{-1}). The parameters are $A = 0.08\ \mathrm{bar}^{-3}\,\mathrm{a}^{-1}$, $m = 3$ and $\sigma_0 = \sqrt{0.1}$ bar.

In absence of snow fall or melting, the volume fraction of ice would satisfy

$$\frac{\partial \varphi}{\partial t} + \mathbf{u} \cdot \nabla \varphi = 0, \tag{10}$$

in a weak sense in the space–time. In other words, φ is constant along the trajectories of the fluid particles which are given by

$$\begin{pmatrix} x'(t) \\ y'(t) \\ z'(t) \end{pmatrix} = \begin{pmatrix} u(x(t), y(t), z(t)) \\ v(x(t), y(t), z(t)) \\ w(x(t), y(t), z(t)) \end{pmatrix}.$$

The strong advantage of the description (9) over an explicit internal boundary condition is that it allows the ice domain to change its topology, we refer for instance to [29] for a review of numerical methods for solving the above equation. Also, the interested reader should note that the transport equation (10) is formulated in the whole cavity Λ although the velocity $\mathbf{u}$ is defined only in the ice domain $\Omega(t)$. As described in [22] and in Section 3.1 hereafter, the transport equation (10) is solved numerically using a forward characteristics method. At each time step, the ice particles move along the trajectories, starting from the ice region, thus there is no need to build an extrapolation of the ice velocity $\mathbf{u}$ in the empty part of the cavity $\Lambda \backslash \Omega(t)$.

On alpine glaciers, solid precipitation exceeds melt in their high-elevation regions and melt is predominant in the lower reaches. The sum of snow fall and ice melt at every point of the glacier is termed the mass balance b, the elevation at which $b = 0$ is the equilibrium line altitude *ELA*, see Fig. 3, and is at around 2950 m a.s.l. on Rhonegletscher nowadays [16]. A source term must be added to the right hand side of (10) to account for accumulation or ablation. Let $b(x,y,z,t)$ be the the water equivalent of the snow or ice height added or removed along the ice–air interface $\Gamma_A(t)$ within one year, the so-called mass balance function. In our model, this quantity is given by climate. For Rhonegletscher, it is based on the model described in [16], which is presented in detail in Section 4.

Given the mass balance function b and following [20], Eq. (10) must be updated as follows:

$$\frac{\partial \varphi}{\partial t} + \mathbf{u} \cdot \nabla \varphi = b \delta_{\Gamma_A(t)}, \tag{11}$$

where δ_{Γ_A} is the density of surface on the ice–air interface Γ_A which satisfies, by definition:

$$\int_V f \delta_{\Gamma_A(t)} dV = \int_{V \cap \Gamma_A(t)} f d\sigma$$

for all volume V and all smooth function f. A physical interpretation can be obtained as follows. Consider an arbitrary volume V contained in the cavity Λ and containing the ice–air interface $\Gamma_A(t)$, see Fig. 4. Integrating (11) over V yields, using the divergence theorem:

$$\frac{d}{dt} \int_V \varphi dV + \int_{\partial V} \mathbf{u} \cdot \mathbf{n} \varphi d\sigma = \int_{\Gamma_A(t) \cap V} b d\sigma, \tag{12}$$

thus the time derivative of the volume of ice contained within V plus the flux of ice entering or leaving V equals the amount of ice added or removed by accumulation or ablation.

To summarize, our goal is to find the volume fraction of ice φ in the whole cavity Λ, the velocity $\mathbf{u}$ and pressure p in the ice domain, satisfying Eqs. (1), (2) and (11). Eq. (1) must be supplemented with the boundary conditions (5)–(7). At the initial time, the volume fraction of ice $\varphi(x,y,z,0)$, or equivalently the initial ice domain $\Omega(0)$, must be provided.

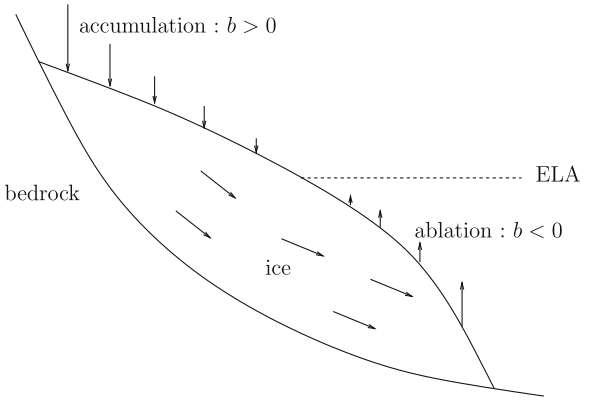

Fig. 3. The mass balance function b (2D figure). When $b > 0$ (respectively $b < 0$), there is accumulation (respectively ablation) of ice at the ice–air interface. The line $b = 0$ marks the altitude of the equilibrium line (*ELA*).

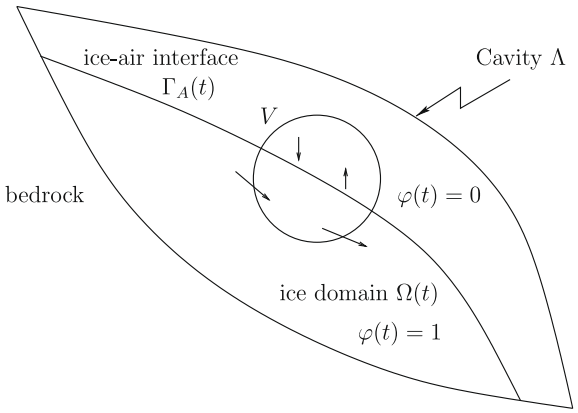

Fig. 4. The mass conservation principle corresponding to (11) in an arbitrary volume V (2D figure) is given by (12).

3. Numerical method

In order to decouple the computation of φ to that of $\mathbf{u}$, p, a time discretization is proposed. Two different space discretizations are then used for solving the transport problem (11) and the nonlinear Stokes problem (1), (2). The transport problem is solved using a structured grid of small cubic cells having size h, with the goal to minimize numerical diffusion. On the other side, since the numerical resolution of the nonlinear Stokes problem is CPU time consuming, an unstructured mesh of tetrahedrons with larger size H is used. The use of two different grids has shown to be very efficient for solving Newtonian [22] and viscoelastic flows [1] with complex free surfaces. A good compromise between accuracy and efficiency is to choose $H \simeq 5h$ with a time step such that the maximum CFL number (velocity times the time step divided by the cells' spacing) is close to 5. The use of an unstructured finite element mesh for the velocity allows complex bedrock geometries to be considered, whereas the use of a structured grid for the volume fraction of ice simplifies the implementation of post-processing procedures to prevent numerical diffusion, see Section 3.2 hereafter. This numerical method has already been presented in [20] to compute the stationary shape of a glacier.

3.1. Time discretization

The time discretization is now presented in details. Let $t^0, t^1, \ldots, t^n, \ldots$ be the discrete times at which approximations are computed. For a given n, assume that an approximation $\varphi^{n-1}(x,y,z)$ of $\varphi(x,y,z,t^{n-1})$ is known for each (x,y,z) in the cavity Λ. We now explain how to compute the new approximation φ^n. Since φ^{n-1} is known, the ice region is defined to be

$$\Omega^{n-1} = \{(x,y,z) \in \Lambda; \varphi^{n-1}(x,y,z) = 1\},$$

the bedrock–ice interface Γ_B^{n-1} and the ice–air interface Γ_A^{n-1} can also be identified. We then solve the nonlinear Stokes problem that is to say find $\mathbf{u}^{n-1} : \Omega^{n-1} \to \mathbb{R}^3$ and $p^{n-1} : \Omega^{n-1} \to \mathbb{R}$ such that

$$-2\mathrm{div}(\mu^{n-1}\varepsilon(\mathbf{u}^{n-1})) + \nabla p^{n-1} = \rho\mathbf{g}, \tag{13}$$

$$\mathrm{div}\,\mathbf{u}^{n-1} = 0, \tag{14}$$

plus zero force boundary condition along Γ_A^{n-1} and slip or no-slip boundary conditions along Γ_B^{n-1} as in (5)–(7). Hereabove, μ^{n-1} is the viscosity computed using (3) with velocity $\mathbf{u}^{n-1}$ instead of $\mathbf{u}$. Then, the transport problem

$$\frac{\partial\varphi}{\partial t} + \mathbf{u}^{n-1}\cdot\nabla\varphi = b\delta_{\Gamma_A^{n-1}},$$

is solved between t^{n-1} and t^n to obtain the new volume fraction of ice φ^n. This transport problem is solved using a first-order splitting scheme in time. The first step of this splitting consists, starting from φ^{n-1}, in solving the transport problem with zero on the right hand side

$$\frac{\partial\varphi}{\partial t} + \mathbf{u}^{n-1}\cdot\nabla\varphi = 0,$$

between t^{n-1} and t^n to obtain the predicted volume fraction of ice $\varphi^{n-1/2}$. A forward characteristic method is advocated, which yields the formula

$$\varphi^{n-1/2}(\mathbf{x} + (t^n - t^{n-1})\mathbf{u}^{n-1}(\mathbf{x})) = \varphi^{n-1}(\mathbf{x}), \tag{15}$$

where we have set $\mathbf{x} = (x,y,z)$. The second step consists, starting from $\varphi^{n-1/2}$, in solving

$$\frac{\partial \varphi}{\partial t} = b\delta_{\Gamma_A^{n-1}},$$

between t^{n-1} and t^n to obtain the new volume fraction of ice φ^n. The Euler scheme is used which yields

$$\varphi^n = \varphi^{n-1/2} + (t^n - t^{n-1})b^n\delta_{\Gamma_A^{n-1}}, \tag{16}$$

with $b^n(x,y,z) = b(x,y,z,t^n)$. The advantage of using this scheme is that it is unconditionally stable, even when the CFL number (velocity times the time step divided by the cells' spacing) is larger than one, see Section 3.2.

3.2. Space discretization with finite elements and structured cells

According to [22,1,3], two different space discretizations will be used to solve the nonlinear Stokes problem (13), (14) and formula (15), (16), see Fig. 5. Since the volume fraction of ice is a discontinuous function across the ice–air interface, numerical diffusion must be reduced as much as possible. For this purpose, the cavity Λ will be covered by a structured grid made out of small cubic cells with size h. Moreover, two post-processing procedures are performed to prevent numerical diffusion – a SLIC method, see for instance [29] – and artificial decompression. These two procedures have already been presented in [22,1,3,20] and will not be expanded here. On the other side, since the numerical resolution of the nonlinear Stokes problem is CPU time consuming, an unstructured finite element mesh made out of tetrahedrons with larger size H will be used, see Fig. 5. The use of finite elements is judicious since the geometry of the cavity is complex, see Fig. 9. Also, the implementation of the boundary conditions (5), (7) is easy within the framework of finite elements methods. It should be stressed that both space discretizations are fixed and do not change with time. As detailed in Section 4.4 of [22], a hierarchic data structure enables an efficient transfer of informations between the structured grid and the finite element mesh.

Assume that the old values φ_{ijk}^{n-1} of the volume fraction of ice are available at each cubic cell with coordinates of center (x_i,y_j,z_k) contained in the cavity Λ. We now present more details of how to compute the new values φ_{ijk}^n. The first task is to define the ice domain on the finite element mesh. For this purpose, values of φ_{ijk}^{n-1} are defined at the vertices of the finite element mesh proceeding as in Section 4.2 of [22]. A tetrahedron is said to be iced if at least one of its four vertices has a volume fraction of ice greater than 0.5. The ice domain Ω_H^{n-1} is then the union of all iced tetrahedrons. Both the ice–air interface $\Gamma_{A,H}^{n-1}$ and the bedrock–ice interface $\Gamma_{B,H}^{n-1}$ can then be identified, the latter being split in two parts, namely $\Gamma_{B,H}^{n-1,NS}$ (no-slip b.c.) and $\Gamma_{B,H}^{n-1,S}$ (slip b.c.). The finite element formulation corresponding to (13), (14) is as follows: Find the ice velocity $\mathbf{u}_H^{n-1} : \Omega_H^{n-1} \to \mathbb{R}^3$ and the ice pressure $p_H^{n-1} : \Omega_H^{n-1} \to \mathbb{R}$ such that $\mathbf{u}_H^{n-1} = \mathbf{0}$ on $\Gamma_{B,H}^{n-1,NS}$ and such that

$$\begin{aligned} &+2\int_{\Omega_H^{n-1}} \mu^{n-1}\varepsilon(\mathbf{u}_H^{n-1}) : \varepsilon(\mathbf{v})dV - \int_{\Omega_H^{n-1}} p_H^{n-1}\operatorname{div}\mathbf{v}dV - \rho\mathbf{g}\int_{\Omega_H^{n-1}} \mathbf{v}dV + \int_{\Gamma_{B,H}^{n-1,S}} \alpha^{n-1}((\mathbf{u}_H^{n-1}\cdot\mathbf{t}_1)(\mathbf{v}\cdot\mathbf{t}_1) \\ &+(\mathbf{u}_H^{n-1}\cdot\mathbf{t}_2)(\mathbf{v}\cdot\mathbf{t}_2))d\sigma + 1.e^{10}\int_{\Gamma_{B,H}^{n-1,S}}((\mathbf{u}_H^{n-1}\cdot\mathbf{n})(\mathbf{v}\cdot\mathbf{n}))d\sigma - \int_{\Omega_H^{n-1}} \operatorname{div}\mathbf{u}_H^{n-1}qdV = 0. \end{aligned} \tag{17}$$

Here $\mathbf{v}$ and q are the velocity and pressure test functions, defined on Ω_H^{n-1} and such that $\mathbf{v} = \mathbf{0}$ on $\Gamma_{B,H}^{n-1,NS}$. Also μ^{n-1} (respectively α^{n-1}) is defined by (3), (respectively (8)) with $\mathbf{u}_H^{n-1}$ in place of $\mathbf{u}$. The term in the third line of (17) corresponds to a penalization of $\mathbf{u}\cdot\mathbf{n} = 0$ on $\Gamma_{B,H}^{n-1,S}$. The solution to the nonlinear problem (17) is sought in the space of continuous functions, piecewise linear on the tetrahedrons of the finite element mesh. A stabilization term is added as in Section 4.3 of [22]. At each time step, several linear Stokes problem are solved, freezing the viscosity and sliding coefficient, until convergence occurs, see [20] for details. The number of iterations required for getting a small discrepancy of the solution (<1%, in practise) decreases with the time step. When the time step is one year, very few iterations are needed, less than 5 in most cases.

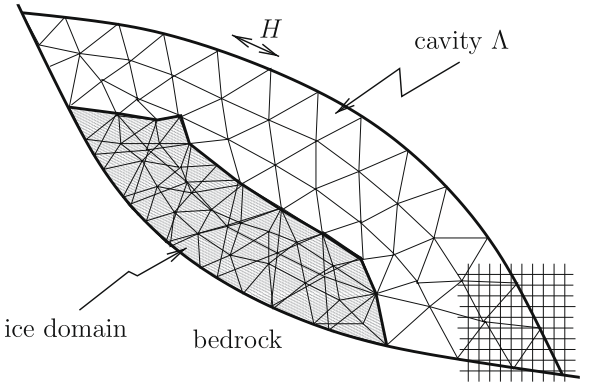

Fig. 5. The two grids (2D figure). The cavity Λ is meshed with unstructured finite elements having size H. Then, at each time step, the ice region is the union of all the elements being filled with ice (pattern area). The cavity is also covered with structured cells having a smaller size $h \simeq H/5$.

Once values of the velocity are available at the vertices of the finite element mesh, values $\mathbf{u}_{ijk}^{n-1}$ are interpolated at the center of each cell *ijk* in the structured grid. Then the two formulas (15), (16) are implemented on the structured cells to obtain new values $\varphi_{ijk}^{n-1/2}$, φ_{ijk}^{n}, respectively. We refer to [22] (respectively [20]) for details concerning the implementation of (15) (respectively (16)).

A validation of the numerical model is proposed in Appendix A. A simple shallow geometry and mass balance function is considered. The steady shape computed using the numerical method is compared to the analytical solution of the Shallow Ice Approximation equation.

4. The mass balance function *b*

The mass balance function b is obtained by simulating accumulation and melt at each point of the glacier surface based on daily weather data. Melt is calculated using a statistical relation between positive air temperature and melt [15]. The parameters involved in the mass balance model have been tuned to fit measured values between 1874 and 2007 optimally [16].

The mass balance b is a function of $(x,y,z(x,y,t),t)$ where $z(x,y,t)$ is the elevation at point (x,y) at time t. Thus, b is a function of (x,y,t) defined by

$$b(x,y,t) = P(x,y,t) - M(x,y,t), \tag{18}$$

where P corresponds to solid precipitation (snow) and M to melt. The function P is given by

$$P = P(x,y,t) = P_{\text{ws}}(t)\left(1 + \frac{dP}{dz}(z(x,y,t) - z_{\text{ws}})\right)c_{\text{prec}}DIST(x,y), \tag{19}$$

where P_{ws} is precipitation measured at a nearby weather station at elevation z_{ws}, dP/dz and c_{prec} are constant coefficients and $DIST$ is the distribution pattern of solid precipitation, calculated from the curvature and slope of the terrain. $DIST$ varies between 0 (complete snow erosion) and 2 (snow deposition). A threshold temperature distinguishes solid from liquid precipitation. M is given by

$$M = M(x,y,t) = \begin{cases} (f_{\text{M}} + r_{\text{ice/snow}}I(x,y,t))T(x,y,t), & \text{if } T(x,y,t) > 0, \\ 0, & \text{else}, \end{cases} \tag{20}$$

where f_{M} and $r_{\text{ice/snow}}$ are constant coefficients, I is the potential direct solar radiation [15] and T is the temperature field computed from measured air temperature T_{ws}:

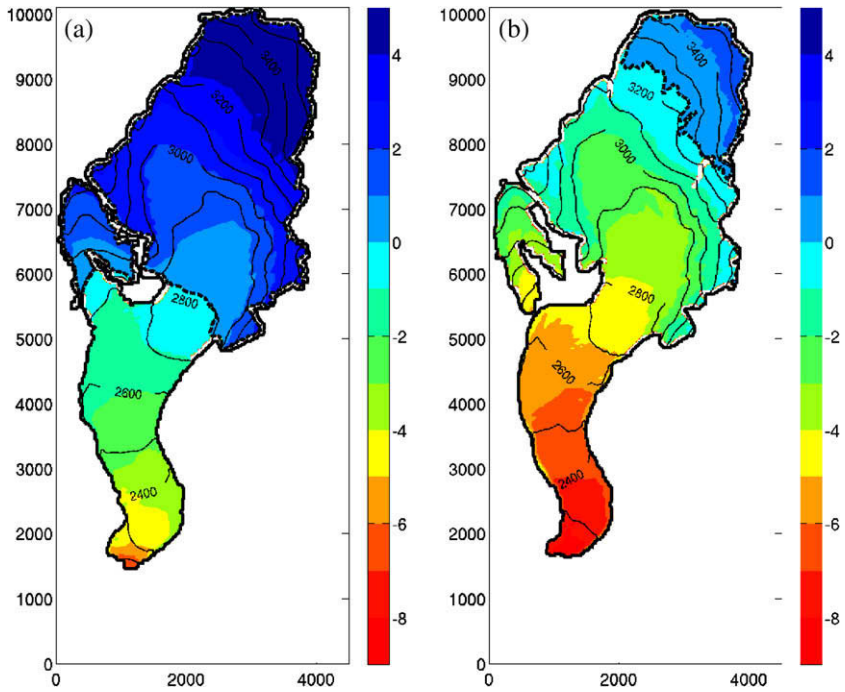

Fig. 6. Mass balance function b for (a) 1977 (mass gain of the glacier) and (b) 2003 (mass loss). The dashed line indicates the equilibrium line. The unit of b is meter water equivalent. The results are shown using a local system of reference. The abscissa of the lower left corner is 671,250 while the ordinate is 157,400 (in the Swiss referential).

$$T(x,y,t) = T_{ws}(t) - 0.006(z(x,y,t) - z_{ws}).$$

The five unknown coefficients f_M, r_{ice}, r_{snow}, c_{prec}, dP/dz involved in (19) and (20) are calibrated according to several types of data [16]: (i) ice volume changes, (ii) point-based mass balance measurements and (iii) water discharge. The function b is computed for each year from 1874 to 2007 and is prescribed in the simulations of Section 5.1. The mass balance function is depicted in Fig. 6 for two extreme years in terms of accumulation and ablation.

Based on a statistical evaluation of 16 regional climate models in seasonal resolution [9], three scenarios for the future change in temperature and precipitation have been considered from 2007 to 2100 [17]: two extreme evolutions and a median scenario. The Scenario 1 (cold–wet) is based on the 2.5% quantile for temperature change and the 97.5% for the precipitation change. The Scenario 2 refers to the median for temperature and precipitation change. The Scenario 3 (warm–dry) is based on the 97.5% quantile for temperature change and the 2.5% for the precipitation change. Each scenario corresponds to a gradual change of P_{ws} and T_{ws}, see Fig. 7. Thus, the function b is calculated over the period 2007–2100 and is used to drive the simulations of Section 5.2.

5. Numerical results

Rhonegletscher, the largest glacier of European Alps during the Last Ice Age, has been thoroughly investigated by glaciologists throughout the last century. As many Alpine glaciers, it has significantly retreated since the end of the Little Ice Age

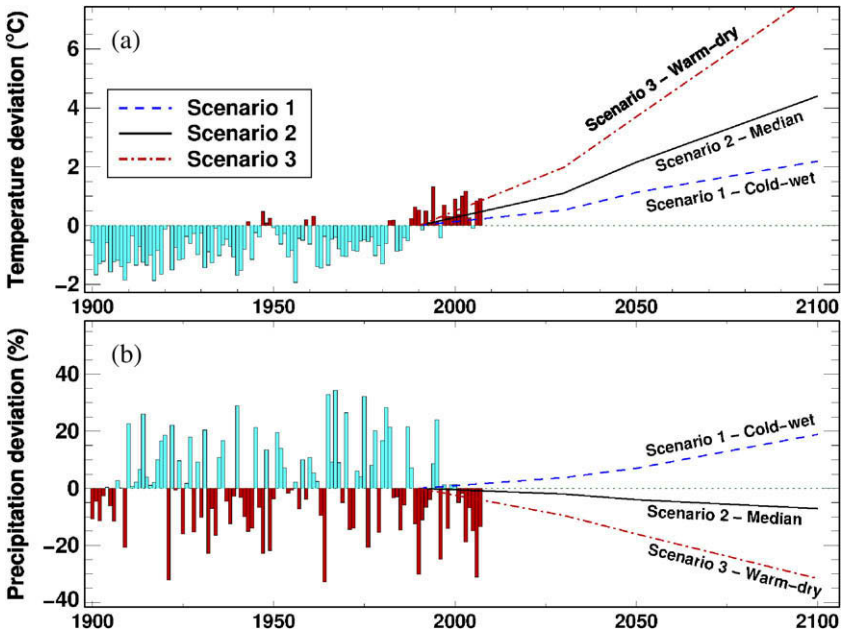

Fig. 7. Deviations of annual (a) mean temperature and (b) precipitation from the climate in 1990. Measured data for the 20th century are displayed by bars, annual changes as assumed by the three climate scenarios are shown until 2100.

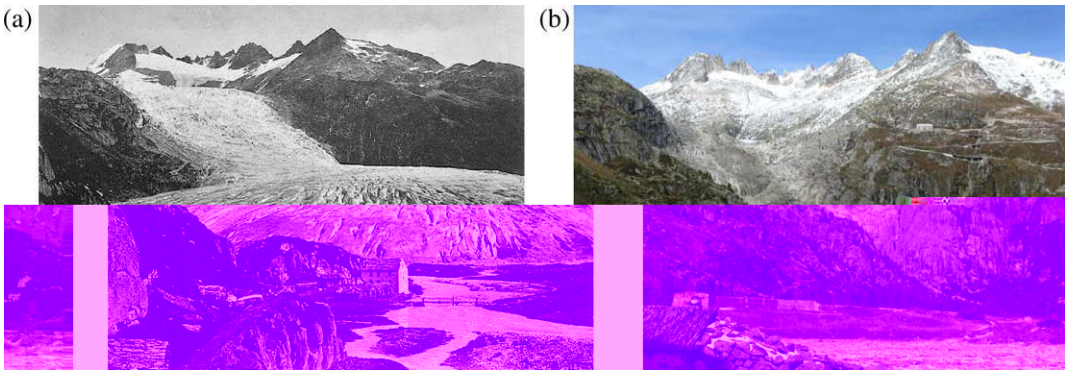

Fig. 8. Pictures of the Rhonegletscher tongue in 1853 (a) and 2008 (b) (source for (a): Alpine Club London).

around 1850 (Fig. 8). It receded 1.2 km between 1880 and the present day [12]. In the following, the glacier retreat between 1874 – when the first measurements are available – and 2007 is simulated. Subsequently, the three different climatic scenarios are considered to predict the surface evolution of the glacier from 2007 to 2100. In all the simulations, the Glen's exponent is set to $m = 3$ (e.g. [14]), and the regularization parameters are set to $\sigma_0 = \sqrt{0.1}$ bar and $s_0 = 0.01$ m a^{-1}.

In the following, the numerical implementation is shortly described. At each vertex (x_i, y_j) of a structured grid in the horizontal rectangle $(0,4000\text{ m}) \times (0,10000\text{ m})$, the bedrock elevation $B(x_i, y_j)$ and the initial ice surface $S(x_i, y_j)$ are provided [7] ($i = 1{,}80$, $j = 1{,}200$). The cell size in the x, y directions is 50 m. A triangular finite element mesh of the bedrock is then generated. A triangular finite element mesh of the top surface of the cavity Λ is also generated by adding 150 m to the initial ice thickness. Then, a Delaunay unstructured mesh of tetrahedrons is generated between the two surfaces using TetMesh-GHS3D [10], thus filling the cavity Λ with tetrahedrons of typical size 50 m. The MeshAdapt remesher [6] is used in order to refine the mesh in the Oz direction only (mesh size 10 m). The final mesh of the cavity has 240,147 vertices, see Fig. 9. The number of vertices of the cavity contained in the initial ice region Ω^0 is 84,161. The block $(0,4000\text{ m}) \times (0,10000\text{ m}) \times (1700\text{ m}, 3600\text{ m})$ containing the cavity Λ is cut into $400 \times 1000 \times 200$ structured cells. The cells which do

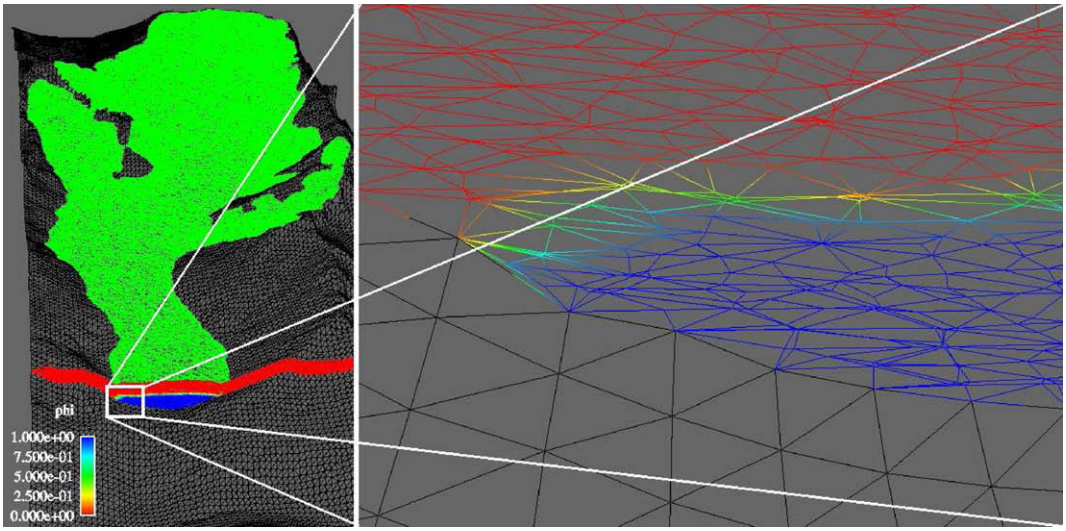

Fig. 9. Cut of the finite element mesh used for Rhonegletscher in 1874. Left: general view. Right: zoom in the white rectangle. The blue section indicates the ice domain (VOF > 0.5) while the red section indicates the air domain (VOF < 0.5). The air–ice interface is materialized by the green color (VOF = 0.5). The mesh size along the bedrock is 50 m while the mesh size along the vertical direction is about 10 m. (For interpretation of the references in color in this figure legend, the reader is referred to the web version of this article.)

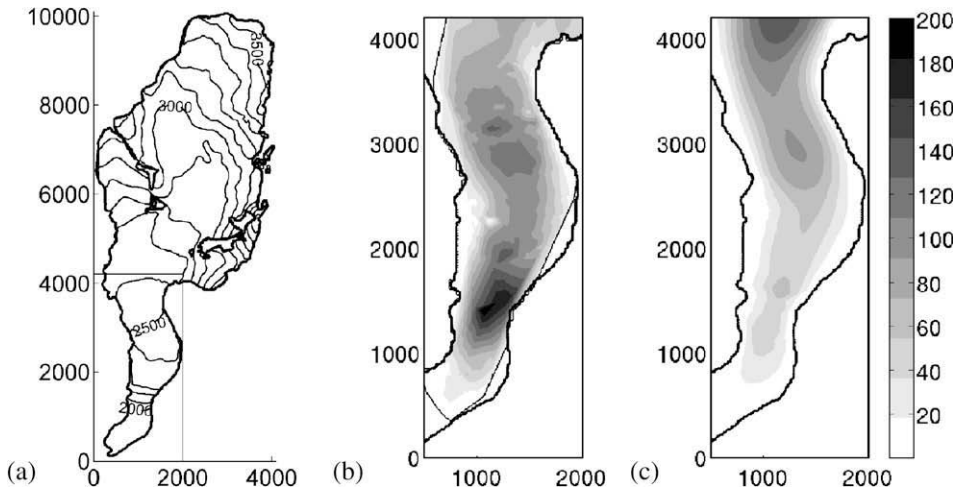

Fig. 10. (a) Outline and level lines of the surface topography of Rhonegletscher on the horizontal plane in 1874. The contour intervals are 100 m. The rectangle corresponds to the surface considered in subfigures (b) and (c). (b) Measured ice surface velocity at the surface from [24] during the period 1875–1885. (c) Computed velocity at the surface in 1874 with no slip condition and $A = 0.08$ bar^{-3} a^{-1}. The color scale indicates surface velocity in m a^{-1}.

not belong to the cavity Λ are not considered in the computation. As in [22] a hierarchic data structure is used in order to activate the cells and decrease the required memory. The time step is half a year. All the computations have been performed on an AMD Opteron 242 CPU with less than 8 Gb memory. About 10 days and 3 days are required for performing the simulations of periods 1874–2007 and 2007–2100, respectively.

5.1. Numerical simulation of Rhonegletscher from 1874 to 2007

The sliding law (7) is subject to higher uncertainties than the flow model (1)–(3), which has been used in several studies in the past. Consequently, the simulation is first performed with no-slip conditions along the bedrock, thus $\Gamma_B^S = \emptyset$ and with $A = 0.08\ \text{bar}^{-3}\ \text{a}^{-1}$ (value taken from [14]). The retreat of the glacier from 1874 to 1900 is significantly too fast in comparison to observations (discussed later in this section). There are several reasons that may explain this difference: (i) Slip boundary conditions are not taken into account along the bedrock, (ii) uncertainty in A, (iii) the bedrock location may be inaccurate in some regions of the glacier and (iv) the ice flow model may not correctly describe glacier dynamics. In order to increase ice discharge towards the glacier terminus and to decrease the misfit with the measurements of glacier retreat we introduce basal sliding. The physical parameters A and C, arising respectively in (3) and (8), are adjusted in order to yield the best fit.

At first, a sliding zone Γ_B^S has to be defined. Ice surface velocity has been measured during the period 1875–1885 by surveying the position of colored stones at the glacier surface [23]. The corresponding velocities have been compiled by [24] and are shown in Fig. 10(b).

The fast ice flow at the glacier terminus during 1875–1885 is remarkable and cannot be explained by ice shear alone. Although the bedrock is very steep, the ice thickness is too shallow (about 100 m) to allow for a surface speed of 200 m a^{-1}. Obviously, sliding is a very important process in this zone of the glacier, this being due to the high slope of the glacier and the texture of the bedrock.

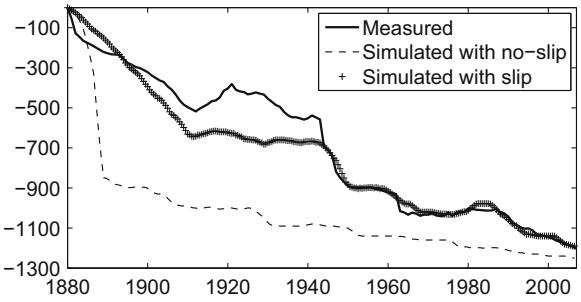

Fig. 11. Comparison of measured and simulated retreat of the glacier tongue between 1880 and 2007. Model runs using no-slip boundary conditions on Γ_B with $A = 0.08$ and runs using slip boundary conditions on Γ_B^S with $A = 0.10$ are shown.

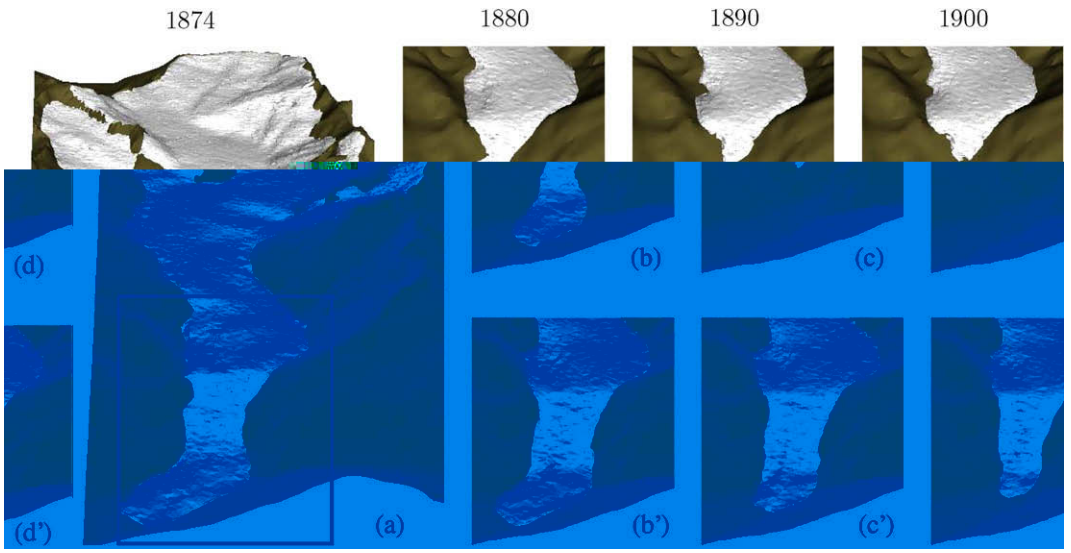

Fig. 12. Simulation of the Rhonegletscher tongue over the period 1874–1900. Left (a): initial glacier extent in 1874. Right, evolution from 1880 to 1900. Top (b, c, d): no-slip on Γ_B and $A = 0.08$; bottom (b', c', d'): slip on Γ_B^S, $A = 0.10$.

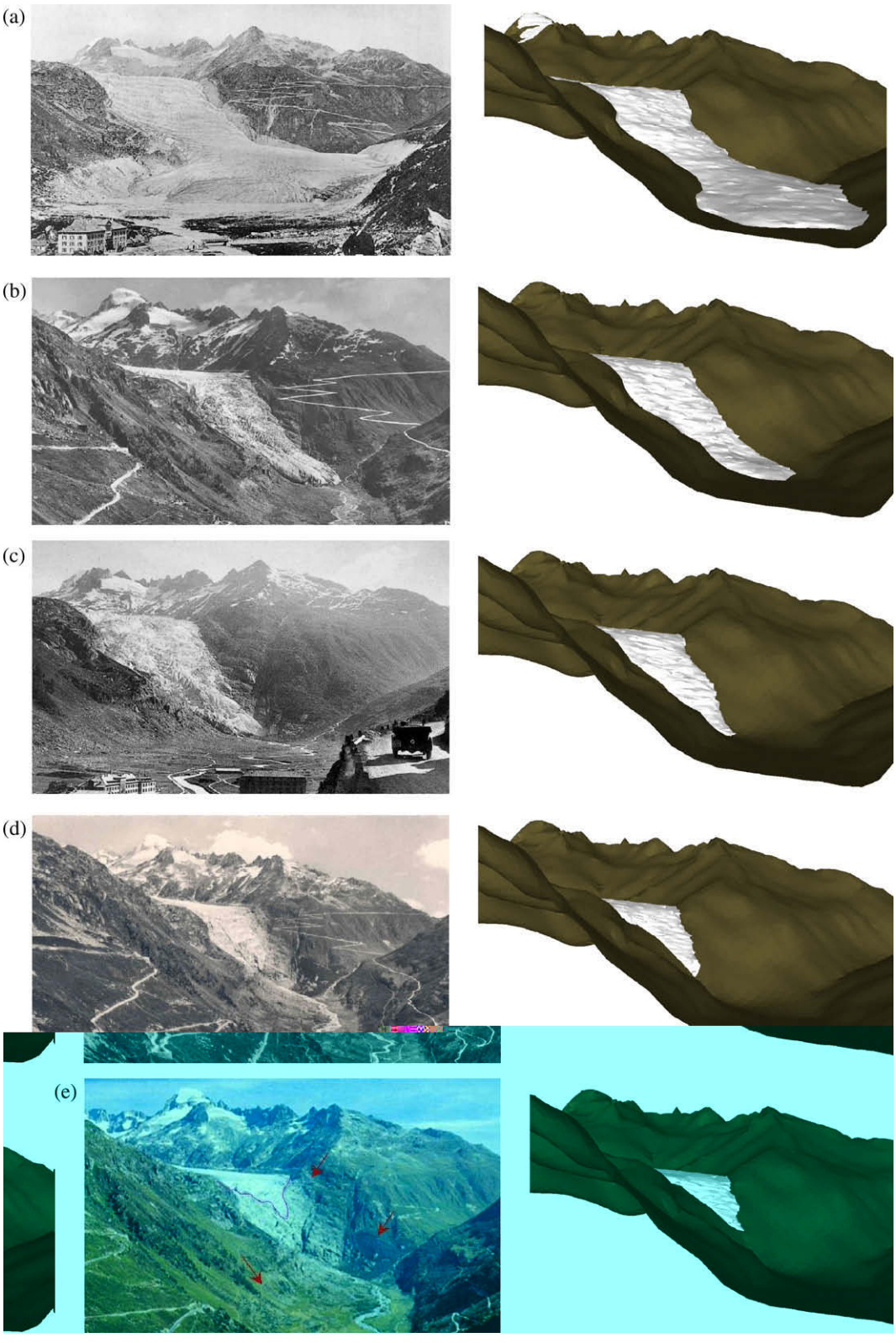

Fig. 13. Photographs of the Rhonegletscher tongue versus simulations in (a) 1874, (b) 1900, (c) 1932, (d) 1960, and (e) 1985 (source for (a) and (e): http://www.unifr.ch/geosciences/geographie/glaciers, (b): Wehrli Verlag, Kilchberg, (c): http://gnosis9.net and (d): Verlag O. Süssli-Jenny Thalwil, http://www.heimatsammlung.de).

The surface geometry of the year 1874 is known from a topographic map. We assume the surface speed measurements [23,24] to correspond to this date. According to previous mechanical evidence, sliding occurs where the measured velocities at the surface are important, the surface slope is steep and the glacier is shallow [26]. The glacier terminus in 1874 combines all of these features, especially the steepest part which is located in between the abscissa 1000 and 2000 (Fig. 10(b)). Moreover, the preliminary simulation (without sliding) shows that the surface velocity in the region south of the *Y-axis* 4000 is overestimated, while it is significantly underestimated in the lower part (Fig. 10(c)). As a consequence, we arbitrarily fix the sliding area as:

$$\Gamma_B^S = \{(x,y,z) \in \Gamma_B; y \leqslant 4000\}. \tag{21}$$

Since measurements of the glacier terminus position are available from [12] between 1880 and 2007 several couples (A,C) have been investigated. $(A,C) = (0.1, 0.3)$ yields the best fit. This combination is used to simulate the evolution of Rhonegletscher from 1874 to 2007. The position of the glacier terminus over time is compared between model runs using no-slip boundary conditions along the bedrock Γ_B, and model runs using slip boundary conditions on the portion Γ_B^S of the bedrock (Figs. 11 and 12). Whereas measured and simulated glacier length fit very well most of the time, there is a slight misfit between 1910 and 1945. This is attributed to a complex ice flow regime in the very steep and shallow glacier tongue during these decades, which could not be captured sufficiently by our model. The simulated extent of the glacier tongue is compared visually to pictures taken in 1874, 1900, 1932, 1960 and 1985 (Fig. 13).

5.2. Numerical simulation of Rhonegletscher from 2007 to 2100

In order to calibrate the physical parameters for simulating in the future, we use a second series of surface speed measurements from 2006 which have been deduced from aerial photographs [24]. Rhonegletscher was globally much slower in 2006 than it was in 1874. Contrary to the year 1874, a stationary computation for the year 2007 without sliding provides surface velocities that fit the measurements well enough and the rate factor $A = 0.08\ \text{bar}^{-3}\,\text{a}^{-1}$ yields the best agreement.

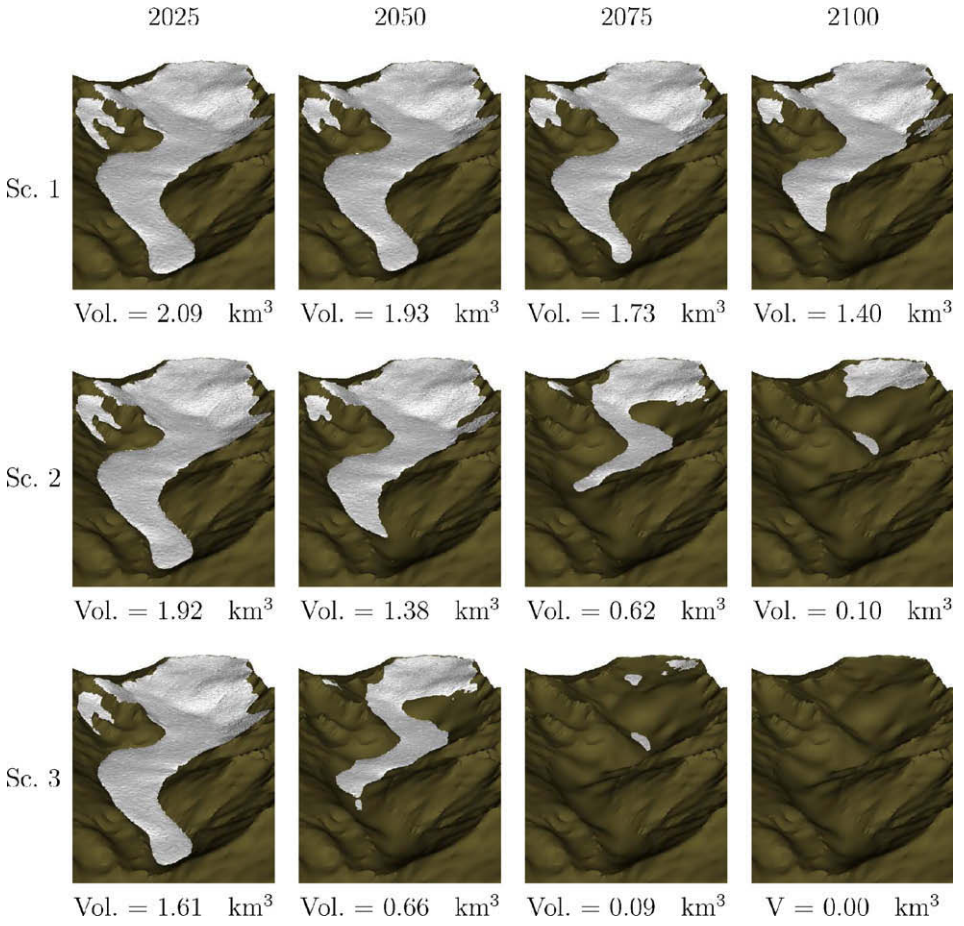

Fig. 14. Simulation over the period 2007–2100 (from left to right). From top to bottom: Scenario 1, 2 and 3. The total ice volume is displayed below each picture.

Starting from the measured glacier geometry in 2007, the numerical simulation of the surface evolution of Rhonegletscher is performed until 2100 using no-slip boundary conditions and $A = 0.08\ \mathrm{bar}^{-3}\ \mathrm{a}^{-1}$. The results of simulations based on the three scenarios presented in Section 4 are displayed in Fig. 14. According to Scenario 2, representing the most probable evolution, the decrease in ice volume until 2050 is moderate (−34% compared to 2007). In the second half of the 21st century a dramatic glacier wastage is expected, leading to the reduction of Rhonegletscher to a small ice field at an elevation of more than 3000 m a.s.l. (Fig. 14). Simulations based on Scenario 3 (warm–dry) even show a complete disappearance of the ice mass by 2075. Scenario 1 (cold–wet), in contrast, only causes minor changes in the glacier extent throughout the 21st century. By 2100 a volume change of only −33% is anticipated. Our model results show a high probability that Alpine glaciers will recede significantly during the next decades. However, the uncertainty of climatic projections is still high and allows for a wide range of possible glacier changes in the near future.

6. Conclusions

The simulation of Rhonegletscher has been performed by combining an ice flow model [20] with a mass balance model [16]. A variety of data collected during the last century enables both models to be adjusted. The three dimensional evolution of the glacier is computed by solving a nonlinear Stokes equation coupled to a volume fraction of ice formulation. The use of two specific meshes for solving diffusion and advection problems divides appropriately the needs of memory and computational time. The numerical method proves to be suitable for accounting for complex glacier geometries, even with separated ice domains (Fig. 14). A simple parameterization of sliding along the bedrock is introduced and significantly increases the power of the model to match observations of glacier retreat.

This combined glacier mass balance and ice-flow model allows us to reconstruct the three dimensional change of alpine glaciers in the past and to make predictions of future glacier wastage under climate change conditions. Our results show that the model accurately reproduces the observed glacier change and ice surface velocities over a time period of more than a century. The forecasts given in the last section confirm the trend of the retreat of Alpine glaciers in the 21st century. The simulation based on the most realistic assumptions for future climate change predicts a dramatic retreat of Rhonegletscher during the 21st century. By 2100 only a small ice field will be left. The model presented in this paper has a high potential to predict the impact of climate change on alpine glaciers during the coming decades. This is of immediate interest for scientists, but also for tourism and economy in alpine environments.

Acknowledgment

We thank Denis Cohen, ETH Zürich and Thomas Zwinger, CSC-Scientific Computing Ltd., Espoo, Finland for advice and remarks concerning slip boundary conditions. We thank Daniel Farinotti and Andreas Bauder, ETH Zürich, for providing us with the bedrock topography and the glacier surface elevation data. We are grateful to Daisuke Nishimura, Hokkaido University, Sapporo, for the ice surface velocity data of Rhonegletscher in 1874 and 2006. We thank Martin Funk, ETH Zürich, for helpful discussions and comments on the manuscript. We thank Katie Dyer for English corrections. Christian Schoof and the unknown reviewer are acknowledged for constructive remarks.

Appendix A. Numerical validation: A comparison between a Shallow Ice Approximation and the full Stokes model

A three-dimensional stationary shallow ice sheet, radial-symmetric of height H_0 and radius $L \gg H_0$ is considered. Since the ratio $\frac{H_0}{L}$ is small, the model can be simplified into a Shallow Ice Approximation [18,21]. When $\sigma_0 = 0$ in Glen's flow law (3), the model reduces to an equation for the ice sheet height $H = H(r)$, see [2]:

$$-\frac{2(\rho\|\mathbf{g}\|)^m A}{m+2}\nabla\cdot\left(H^{m+2}\|\nabla H\|^{m-1}\nabla H\right) = b(r), \tag{A.1}$$

where the mass balance function b is a function of the radial coordinate defined by $r = \sqrt{x^2+y^2}$. When b is given by

$$b(r) = \frac{\alpha}{r}\left(\left(\frac{r}{L}\right)^{\frac{1}{m}} + \left(1-\frac{r}{L}\right)^{\frac{1}{m}} - 1\right)^m + \frac{\alpha}{L}\left(\left(\frac{r}{L}\right)^{\frac{1}{m}} + \left(1-\frac{r}{L}\right)^{\frac{1}{m}} - 1\right)^{m-1}\left(\left(\frac{r}{L}\right)^{\frac{1}{m}-1} - \left(1-\frac{r}{L}\right)^{\frac{1}{m}-1}\right), \tag{A.2}$$

with $\alpha > 0$, then the analytic solution of (A.1) such that $H(L) = 0$ is given by [2]:

$$H(r) = H_0\left(1 - \frac{m}{m-1}\left(\left(\frac{r}{L}\right)^{1+\frac{1}{m}} - \left(1-\frac{r}{L}\right)^{1+\frac{1}{m}} + 1 - \left(1+\frac{1}{m}\right)\frac{r}{L}\right)\right)^{\frac{m}{2m+2}}, \tag{A.3}$$

where

$$H_0 = \left(\frac{m-1}{m+1}CL\alpha^{\frac{1}{m}}\right)^{\frac{m}{2m+2}} \quad \text{and} \quad C = \left(\frac{2m+2}{m}\right)(m+2)^{\frac{1}{m}}(2(\rho g)^m A)^{-\frac{1}{m}},$$

where $H_0 = H(0)$ is the maximum ice sheet thickness.

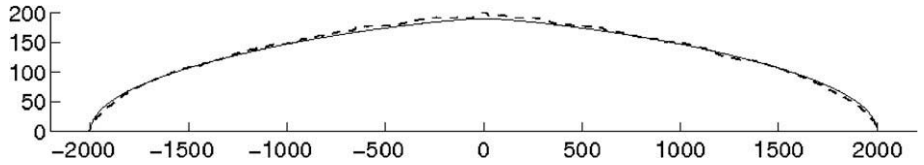

Fig. A.1. Numerical validation with a shallow ice sheet. Section of the steady shape with respect to the radial distance r. Dashed line: computed shape, continuous line: analytic solution of shallow ice approximation (A.3).

The ice thickness function H can be associated to the volume fraction of ice φ by using Eqs. (15) and (16) of [20].

In the following experiment, we set $L = 2000$ m and α so that we obtain $H_0 \simeq 190$ m. In Glen's law (3), we set $m = 3$, $A = 0.08\ \text{bar}^{-3}\ \text{a}^{-1}$ and $\sigma_0 = \sqrt{0.1}$ bar. A tetrahedral mesh of the cavity Λ of size 5000 m $\times$ 5000 m $\times$ 200 m containing the radial ice sheet is generated. The mesh has 153,796 vertices while the structured grid is composed by $500 \times 500 \times 20$ cells. At initial time the cavity contains no ice, $\Omega^0 = \emptyset$. The simulation is performed with no-slip conditions along the flat base. The time step is one year, a steady state geometry is observed after 1000 years. The steady shape computed and the exact solution (A.3) are drawn together in Fig. A.1 for being compared. The well fit between these two curves validates the numerical method presented in Section 3.

References

[1] A. Bonito, M. Picasso, M. Laso, Numerical simulation of 3D viscoelastic flows with free surfaces, J. Comput. Phys. 215 (2) (2006) 691–716.
[2] E. Bueler, Construction of Steady State Solutions for Isothermal Shallow Ice Sheets. Technical Report 03-02, UAF DMS, December 2003.
[3] A. Caboussat, M. Picasso, J. Rappaz, Numerical simulation of free surface incompressible liquid flows surrounded by compressible gas, J. Comput. Phys. 203 (2) (2005) 626–649.
[4] J. Colinge, J. Rappaz, A strongly nonlinear problem arising in glaciology, M2AN Math. Model. Numer. Anal. 33 (2) (1999) 395–406.
[5] A. Deponti, V. Pennati, L. de Biase, V. Maggi, F. Berta, A new fully three-dimensional numerical model for ice dynamics, J. Glaciol. 52 (178) (2006) 365–376.
[6] S.A.S. Distene, Pôle Teratec – BARD-1, Domaine du Grand Rué, 91680 Bruyères-le-Chatel, France. MeshAdapt: A Mesh Adaptation Tool, User's manual Version 3.0, 2003.
[7] D. Farinotti, M. Huss, A. Bauder, M. Funk, M. Truffer. A method to estimate ice volume and ice thickness distribution of alpine glaciers. J. Glaciol. 55(191) (2009) 422–430.
[8] A.C. Fowler, A theoretical treatment of the sliding of glaciers in the absence of cavitation, Philos. Trans. Roy. Soc. London Ser. A 298 (1445) (1980/81) 637–681.
[9] C. Frei, Die Klimazukunft der Schweiz, in: Klimaänderung und die Schweiz 2050 – Erwartete Auswirkungen auf Umwelt, Gesellschaft und Wirtschaft, Beratendes Organ für Fragen der Klimaänderung (OcCC), 2007, pp. 12–16. http://www.occc.ch.
[10] P. Frey, P.-L. George, Mesh generation, second ed., ISTE, London, 2008. Application to finite elements.
[11] O. Gagliardini, D. Cohen, P. Raback, T. Zwinger, Finite-element modeling of subglacial cavities and related friction law, J. Geophys. Res. 112 (2007).
[12] The Swiss Glaciers, 1880–2002/03, Technical Report 1-124, Yearbooks of the Cryospheric Commission of the Swiss Academy of Sciences (SCNAT), 1881–2008. Published since 1964 by Laboratory of Hydraulics, Hydrology and Glaciology (VAW) of ETH Zürich.
[13] J.W. Glen, The flow law of ice, IUGG/IAHS Symposium of Chamonix IAHS Publication, 47:171G 183, 1958.
[14] G.H. Gudmundsson, A three-dimensional numerical model of the confluence area of unteraargletscher, Bernese Alps, Switzerland, J. Glaciol. 45 (150) (1999) 219–230.
[15] R. Hock, A distributed temperature-index ice- and snowmelt model including potential direct solar radiation, J. Glaciol. 45 (149) (1999) 101–111.
[16] M. Huss, A. Bauder, M. Funk, R. Hock, Determination of the seasonal mass balance of four alpine glaciers since 1865, J. Geophys. Res. 113 (2008) F01015.
[17] M. Huss, D. Farinotti, A. Bauder, M. Funk, Modelling runoff from highly glacierized alpine drainage basins in a changing climate, Hydrol. Processes 22 (19) (2008) 3888–3902.
[18] K. Hutter, Theoretical Glaciology, Reidel, 1983.
[19] IPCC, Climate Change 2007, The Physical Scientific Basis. Contributions of Working Group I to the Fourth Assessment Report of the Intergovernmental Panel on Climate Change, Technical Report, WMO/UNEP, Cambridge University Press, 2007.
[20] G. Jouvet, M. Picasso, J. Rappaz, H. Blatter, A new algorithm to simulate the dynamics of a glacier: theory and applications, J. Glaciol. 54 (2008) 801–811.
[21] E. Le Meur, O. Gagliardini, T. Zwinger, J. Ruokolainen, Glacier flow modelling: a comparison of the Shallow Ice Approximation and the full-Stokes solution, Comptes Redues Phys. 5 (7) (2004) 709–722.
[22] V. Maronnier, M. Picasso, J. Rappaz, Numerical simulation of three-dimensional free surface flows, Int. J. Numer. Methods Fluids 42 (7) (2003) 697–716.
[23] P.L. Mercanton, Vermessungen am Rhonegletscher, 1874–1915, Neue Denkschriften der Schweizerischen Naturforschenden Gesellschaft 52 (1916).
[24] D. Nishimura, Changes in surface flow speed over the past 100 years (Rhonegletscher, Swiss Alps), Master thesis, Graduate School of Environmental Science, Hokkaido University, 2008.
[25] S. Osher, R.P. Fedkiw, Level set methods: an overview and some recent results, J. Comput. Phys. 169 (2) (2001) 463–502.
[26] W.S.B. Paterson, The Physics of Glaciers, third ed., Pergamon, New York, 1994. p. 480.
[27] M. Picasso, J. Rappaz, A. Reist, M. Funk, H. Blatter, Numerical simulation of the motion of a two dimensional glacier, Int. J. Numer. Methods Eng. 60 (2004) 995–1009.
[28] A. Pralong, M. Funk, A level-set method for modeling the evolution of glacier geometry, J. Glaciol. 50 (171) (2004) 485–491.
[29] R. Scardovelli, S. Zaleski, Direct numerical simulation of free-surface and interfacial flow, Ann. Rev. Fluid Mech. 31 (7) (1999) 567–603.
[30] C. Schoof, The effect of cavitation on glacier sliding, Royal Soc. London Proc. Ser. A 461 (2005) 609–627.
[31] C. Schoof, Coulomb friction and other sliding laws in a higher-order glacier flow model, M3AS, accepted for publication.
[32] S. Sugiyama, A. Bauder, M. Funk, C. Zahno, Evolution of Rhonegletscher, Switzerland, over the past 125 years and in the future: application of an improved flowline model, Annals Glaciol. 46 (2007) 268–274.
[33] A. Vieli, M. Funk, H. Blatter, Tidewater glaciers: frontal flow acceleration and basal sliding, Annals Glaciol. 31 (2000) 217–221. 5 January.
[34] J. Wallinga, R.S.W. van de Wal, Sensitivity of Rhonegletscher, Switzerland, to climate change: experiments with a one-dimensional flowline model, J. Glaciol. 44 (147) (1998) 383–393.